Agricultural and Forest Meteorology 304-305 (2021) 108424

Contents lists available at ScienceDirect

Agricultural and Forest Meteorology

journal homepage: www.elsevier.com/locate/agrformet

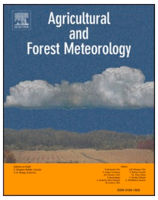

Constraining global terrestrial gross primary productivity in a global carbon assimilation system with OCO-2 chlorophyll fluorescence data

Jun Wang [a,b], Fei Jiang [a,b,*], Hengmao Wang [a,b], Bo Qiu [a,b], Mousong Wu [a,b], Wei He [a,b], Weimin Ju [a,b], Yongguang Zhang [a,b], Jing M. Chen [a,c], Yanlian Zhou [b]

[a] *International Institute for Earth System Science, Nanjing University, Nanjing, Jiangsu 210023, China*

[b] *Jiangsu Provincial Key Laboratory of Geographic Information Science and Technology, Key Laboratory for Land Satellite Remote Sensing Applications of Ministry of Natural Resources, School of Geography and Ocean Science, Nanjing University, Nanjing, Jiangsu 210023, China*

[c] *Department of Geography and Program in Planning, University of Toronto, Toronto, Ontario M5S3G3, Canada*

ARTICLE INFO

Keywords:
GPP
V_{cmax}^{25}
OCO-2 SIF
Carbon assimilation system

ABSTRACT

The gross primary productivity (GPP) is the largest carbon flux in the terrestrial carbon cycle. Constraining GPP is critical for understanding the terrestrial carbon sources and sinks. In this study, we attempted to constrain the terrestrial GPP at regional to global scales through optimizing the key photosynthetic parameter (the carboxylation capacity at 25 °C, V_{cmax}^{25}) using solar-induced chlorophyll fluorescence (SIF) observations from the Orbiting Carbon Observatory-2 (OCO-2). The optimization was made within the Global Carbon Assimilation System (GCAS), in which the Boreal Ecosystem Productivity Simulator (BEPS) model was used to simultaneously simulate the global GPP and SIF in the process-based manner. Optimized V_{cmax}^{25} shows a distinguishable spatial pattern, with the largest values over the crop regions. After optimization, V_{cmax}^{25} of crop is significantly increased. Importantly, the optimized V_{cmax}^{25} of different plant functional types (PFTs) show unambiguous seasonal variations. With these optimized V_{cmax}^{25}, the simulated global GPP in 2015–2016 amounts to 119.1 PgC yr^{-1}, close to the median value (121.3 PgC yr^{-1}) of the observation-based estimates. Global GPP decreases by 8.3% relative to the value simulated using prior V_{cmax}^{25}. In detail, GPP of crops increases by 16.4%, but it decreases over the other PFT regions, ranging from −4.4% over grasses to −34.0% over deciduous needleleaf forests. The spatiotemporal variations in the optimized PFT-dependent V_{cmax}^{25} also reshape the seasonal cycle in GPP. We regard that it is an effective pathway to constrain GPP based on the satellite SIF and the process-based assimilation system, which can provide us an opportunity to better understand the terrestrial and global carbon cycle.

1. Introduction

The gross primary productivity (GPP), as the largest terrestrial carbon flux, is caused by the photosynthesis of terrestrial vegetation, in which atmospheric carbon dioxide (CO_2) is fixed into organic compounds. Based on the simulations involved in the North American Carbon Program (NACP), Huntzinger et al. (2012) suggested that there are larger inter-model spreads in the estimates of gross primary productivity (GPP) and respiration than in estimates of net ecosystem productivity (NEP). Beer et al. (2010) estimated global GPP at 123 ± 8 Pg C yr^{-1}, mainly based on eddy covariate flux data. In the TRENDY project, under the same protocol and same climate forcing and land use datasets, the ensemble mean of global GPP estimated by 10 process-based terrestrial biosphere models was 133 ± 15 Pg C yr^{-1} (Piao et al., 2013), higher than the estimate of Beer et al. (2010). Additionally, in the second phase of the Inter-Sectoral Impact Model Intercomparison Project (ISIMIP2a), terrestrial biosphere models under four different meteorological forcing datasets also produced the large inter-model different terrestrial GPP, ranging from 98 to 141 Pg C yr^{-1} averaged for 1981–2000 (Ito et al., 2017). These large differences in the global GPP estimates can originate from different forcing datasets, parameterizations, processes considered, which make the surprising differences in model representation of responses of photosynthesis to CO_2 concentration, temperature, soil moisture, and vapor pressure deficit (Rogers, 2014; Rogers et al., 2014). Therefore, it is critical to develop a method for constraining terrestrial GPP to reduce the uncertainties in NEP and better understand the

---

* Corresponding author.
E-mail addresses: wangjun@nju.edu.cn (J. Wang), jiangf@nju.edu.cn (F. Jiang).

https://doi.org/10.1016/j.agrformet.2021.108424
Received 25 May 2020; Received in revised form 2 April 2021; Accepted 5 April 2021

terrestrial carbon cycle.

Recent satellite-based observations of solar-induced chlorophyll fluorescence (SIF) provide a new opportunity to map the spatiotemporal patterns of terrestrial GPP (Frankenberg et al., 2011; Guanter et al., 2014; Hilton, 2018; Joiner et al., 2011; Zhang et al., 2014b). In the molecular machinery, chloroplasts capture photons from the sun to transfer CO_2 molecules into carbon and oxygen. Chloroplasts also emit photons to release excess energy and prevent harmful energy accumulation. These emitted photons are known as SIF, which is directly associated with photosynthesis (Frankenberg et al., 2011; Hilton, 2018). Many studies have suggested that a simple linear correlation exists between GPP and SIF (Frankenberg et al., 2011; Guanter et al., 2014). Therefore, SIF has been used to constrain the global GPP distributions in the recent terrestrial carbon cycle research (Bacour et al., 2019; Koffi et al., 2015; MacBean et al., 2018; Norton et al., 2019; Parazoo et al., 2014).

Satellite-based SIF is generally used to constrain global terrestrial GPP in two ways. The first is mainly based on the linear relationship between SIF and GPP. For instance, Parazoo et al. (2014) used the global observations of SIF from the Greenhouse gases Observing SATellite (GOSAT) to constrain the distribution of the ensemble mean of GPP from DGVMs through an optimal estimation method. MacBean et al. (2018) optimized the GPP parameters based on the assumption that the linear relationship between SIF and GPP can hold from daily to monthly time steps.

However, the relationship between SIF and GPP can be affected by canopy structure (Zhang et al., 2020) and vary with temporal scales (Damm et al., 2015), which limit the applicability of GPP linearly estimated from satellite SIF data as observations to constrain GPP and parameter estimates. The direct assimilation of satellite observed SIF into process-based models, which can be able to simulate both GPP and canopy SIF, might avoid this problem. Therefore, the second pathway takes a process-based approach in which key parameters affecting GPP simulation in a terrestrial biosphere model were constrained through minimizing the difference between simulated and satellite observed SIF. Koffi et al. (2015) used this approach to investigate the usefulness of SIF in constraining GPP within the carbon cycle data assimilation system (CCDAS). More recently, Norton et al. (2019) and Bacour et al. (2019) used the terrestrial biosphere models to simultaneously simulate GPP and SIF. Then they assimilated SIF from the Orbiting Carbon Observatory-2 (OCO-2) into terrestrial biosphere models to better estimate GPP through model parameter optimization.

In this study, using the Boreal Ecosystem Productivity Simulator (BEPS) (Chen et al., 2012) innovated with an explicit process-based SIF module (Qiu et al., 2019), we explore a method to constrain the terrestrial GPP through optimizing the carboxylation capacity at 25 °C (V_{cmax}^{25}), a key parameter determining photosynthesis rates, under the framework of the Global Carbon Assimilation System (GCAS) (Zhang et al., 2015a) based on the OCO-2 SIF. This assimilation module will be an important component in GCAS, which was designated to assimilate multi-source observations including the surface in situ CO_2 and satellite-based XCO_2 products. In this module, we attempt to optimize PFT-dependent V_{cmax}^{25} in space and time, based on the separation of global land, which is different from the previous studies (Bacour et al., 2019; Norton et al. 2019). In this paper, we will illustrate the method, assess its performance, and investigate the changes between the prior and posterior V_{cmax}^{25} and GPP.

This paper is organized as follows: Section 2 presents the main methodologies of the SIF module and assimilation and datasets used. The optimization performance, spatiotemporal patterns of the optimized V_{cmax}^{25}, and constrained GPP are illustrated in Sect. 3. Discussions and concluding remarks are presented in Sect. 4 and Sect. 5, respectively.

Table 1
Default V_{cmax}^{25} values of different plant functional types (PFTs) in the BEPS model.

No.	PFTs in BEPS	Abbre.	Default V_{cmax}^{25} in BEPS (μmol $m^{-2}s^{-1}$)
1	Evergreen needleleaf	ENF	62.5 ± 24.7
2	Deciduous needleleaf	DNF	39.1 ± 11.7
3	Deciduous broadleaf	DBF	57.7 ± 21.2
4	Evergreen broadleaf	EBF	29.0 ± 7.7
5	Mix	Mix	66.0 ± 20.0
6	Shrub	Shrub	57.9 ± 19.6
7	Grass	Grass	48.0 ± 15.0
8	Crop	Crop	84.5 ± 36.6

2. Methods and datasets

2.1. BEPS model with process-based SIF module

The BEPS model was originally developed for boreal ecosystems, and has been expanded for the global GPP simulations (Chen et al., 1999; Chen et al., 2012). The model adopts the strategy of sunlit-shaded leaf stratification (Norman, 1982) when modeling the canopy-level photosynthesis. It contains eight plant functional types (PFTs) as follows: evergreen needleleaf forests (ENF), deciduous needleleaf forests (DNF), deciduous broadleaf forests (DBF), evergreen broadleaf forests (EBF), mixed forests (Mix), shrub, grass, and crops (Table 1). The geographical distribution of the dominant PFT in the BEPS model is shown in Fig. S1. The GPP in each grid is aggregated as the area-weighted average of individual PFTs. BEPS model is flexible at different time steps and spatial resolutions.

A SIF module was recently developed in the BEPS model (Qiu et al., 2019). The SIF was first estimated at the leaf level, and then up-scaled to the canopy level. Finally, the SIF values in each grid is also calculated as the area-weighted average of individual PFTs. The formulas for SIF calculation are briefly described here. More details about the SIF module can be referred to Qiu et al. (2019).

At the leaf level, the flux of emitted fluorescence (SIF_e) can be expressed as:

$$SIF_e = APAR \cdot \varnothing_F \tag{1}$$

where $APAR$ is the absorbed photosynthetically active radiation, calculated by the radiation transfer scheme in BEPS model (Chen et al., 1999). $\varnothing_F$ is the fluorescence yield, which can be further written as:

$$\varnothing_F = \frac{k_F}{k_F + k_D + k_N} \cdot (1 - \varnothing_P) \tag{2}$$

in which k_D and k_N represent the fractional heat loss in light-adapted and dark-adapted conditions, respectively. k_F is the fractional energy for fluorescence. $\varnothing_P$ represents the absorbed energy transferred via photochemistry.

In above equation, k_D and k_F have the respective values of 0.95 and 0.05. Parameter k_N is derived following a function of the degree of light saturation $\chi = 1 - \varnothing_P / \varnothing_{P_0}$ (van der Tol et al., 2014):

$$k_N = k_N^0 \cdot \frac{(1+\beta)\chi^\alpha}{\beta + \chi^\alpha} \tag{3}$$

where $\varnothing_{P_0}$ represents the maximum photochemical yield as observed under dark adapted, low light conditions; $k_N^0 = 2.48$, $\alpha = 2.83$, and $\beta = 0.114$ according to van der Tol et al. (2014).

The $\varnothing_P$ is calculated as:

$$\varnothing_P = \varnothing_{P_0} \cdot \frac{J_e}{J_0} \tag{4}$$

where J_e and J_0 represent the actual and maximum possible electron transport rates. The parameters hold the same values for the sunlit and shaded leaves.

Then, we up-scale the SIF_e at the leaf level to the canopy level. Due to the different illumination between sunlit and shaded leaves, the canopy-leaving fluorescence (SIF_c) deals with the sunlit and shaded leaves separately:

$$SIF_c = SIF_{sun} + SIF_{shad} \tag{5}$$

where SIF_{sun} and SIF_{shad} indicate the sunlit and shaded parts of fluorescence, which will be further calculated with the fluorescence extinction and scattering in the canopy (Qiu et al., 2019).

In this study, BEPS was run at 1-hour time steps and 1° × 1° horizontal resolution. The leaf area index (LAI) used in the model was generated by fusion of the Moderate Resolution Imaging Spectroradiometer (MODIS) and Advanced Very High Resolution Radiometer (AVHRR) (Liu et al., 2012). This dataset was at 8-day intervals with the original 8-km spatial resolution. And the climate-forcing datasets were constructed from the ECMWF ERA-Interim (Dee et al., 2011).

2.2. OCO-2 SIF observations and uncertainty

In this study, we took the SIF retrievals from OCO-2 (Sun et al., 2018) as the observations in the data assimilation system. The OCO-2 was launched in July 2014, which flies in a sun-synchronous orbit and has the local overpass at 1:30 pm. Its spectrometers collect 24 spectra per second with the nominal spatial resolution of 1.3 × 2.25 km^2 in each spectrum at nadir.

The OCO-2 SIF datasets used here are OCO2_L2_Lite_SIF.8r, where the SIF and its related fields are stored on a daily basis. The SIF in each file is the instantaneous retrievals at the local overpass time, including two values at 757 nm (denoted as 'SIF_757nm') and 771 nm (denoted as 'SIF_771nm'). These two retrievals are preformed independently, and SIF_757 nm is approximately 1.5 times higher than SIF_771 nm (Sun et al., 2018). In this study, we only used SIF_757 nm because of the treatment of BEPS SIF module. Given that the mode of the nadir typically provides the better signal-to-noise ratio and higher horizontal resolution soundings than the mode of glint, we only retained the SIF retrievals under the nadir mode at the preprocessing stage.

To be consistent with the resolution of the assimilation system, the SIF retrievals were then aggregated into 1° × 1° resolution. In each grid, we calculated the averaged SIF values if there were at least three soundings in that day.

The settings of observational uncertainties are important in the data assimilation system. In this study, we calculated the uncertainties in each grid according to the method of Norton et al. (2019). The formula is as follows:

$$\sigma = \frac{1}{2} \cdot \frac{\sum \sigma_e}{n} \tag{6}$$

where σ_e is the single measurement precision error of each sounding, and n represents the total number of soundings in the grid.

2.3. Data assimilation method and implementation

The assimilation module used to constrain global terrestrial GPP in this study is newly developed under the framework of GCAS (Zhang et al., 2014a, 2015a). GCAS was originally used to optimize the terrestrial carbon flux based on the prior land–atmosphere carbon fluxes by BEPS offline simulations and the atmospheric CO$_2$ concentration observations preprocessed in the CarbonTracker (Peters et al., 2007).

In this newly developed assimilation module, we adopted the approach of a Local Ensemble Transform Kalman Filter (LETKF) (Hunt et al., 2007). In the BEPS model, photosynthetic rates of sunlit and shaded leaves are simulated using biochemical model developed by Farquhar et al. (1980). Owing to the linear relationship between J_{max} and V_{cmax} ($J_{max} = 2.39 \cdot V_{cmax} - 14.2$) (Medlyn et al., 1999), the parameter of V_{cmax}^{25} is the key determinant of the gross photosynthetic rates. Fluorescence emitted by leaves is closely linked to photochemical efficiency and electron transport rate (Genty et al., 1989; Weis and Berry, 1987). The ground measurements at Harvard Forest also confirmed the close link between chlorophyll fluorescence and electron transport rate at the canopy level (Yang et al., 2015). As in the SIF module, actual and the maximum possible electron transport rates are two key parameters determining SIF emission. They are both tightly related to V_{cmax}^{25} (Chen et al., 1999). Hence, SIF should have a close link with V_{cmax}^{25}. With satellite SIF as observations, Zhang et al. (2018) successfully optimized V_{cmax}^{25} of crops for the US Corn Belt region and found that optimized V_{cmax}^{25} exhibited large spatial and temporal variations. The optimization of V_{cmax}^{25} improved the simulation of cropland GPP. Our sensitivity experiments show that both GPP and SIF simulated by BEPS are sensitive to V_{cmax}^{25} and the former has higher sensitivity than the latter (Fig. S2).

Therefore, we set the state vector as:

$$\boldsymbol{x} = \left\{ V_{cmax}^{25} \right\} \tag{7}$$

where the V_{cmax}^{25} is PFT-dependent. There are up to eight PFTs in each grid in the current BEPS version (there are up to eight V_{cmax}^{25} in each grid). The process of optimization is to minimize a cost function as:

$$J(\boldsymbol{x}) = \left(\boldsymbol{x} - \overline{\boldsymbol{x}}^b\right)^T \left(\boldsymbol{P}^b\right)^{-1} \left(\boldsymbol{x} - \overline{\boldsymbol{x}}^b\right) + [(\boldsymbol{y}^o - H(\boldsymbol{x})]^T \boldsymbol{R}^{-1} [(\boldsymbol{y}^o - H(\boldsymbol{x})] \tag{8}$$

where $\boldsymbol{P}^b$ and $\boldsymbol{R}$ represent the background and observational error covariance matrix. $\boldsymbol{R}$ is here prescribed with a diagonal matrix with the variance of the OCO-2 SIF uncertainty. $\boldsymbol{y}^o$ and $H(\boldsymbol{x})$ denote the OCO-2 observed SIF and BEPS simulated SIF, respectively. For the background ensemble:

$$\overline{\boldsymbol{x}}^b = k^{-1} \sum_{i=1}^{k} \boldsymbol{x}^{b(i)},$$

$$\boldsymbol{P}^b = (k-1)^{-1} \sum_{i=1}^{k} \left(\boldsymbol{x}^{b(i)} - \overline{\boldsymbol{x}}^b\right) \left(\boldsymbol{x}^{b(i)} - \overline{\boldsymbol{x}}^b\right)^T = (k-1)^{-1} \boldsymbol{X}^b \left(\boldsymbol{X}^b\right)^T \tag{9}$$

where k denotes the ensemble size.

In LETKF, there is a transformation that $\boldsymbol{x} = \overline{\boldsymbol{x}}^b + \boldsymbol{X}^b \boldsymbol{w}$, where $\boldsymbol{w}$ is a Gaussian random vector with mean $\boldsymbol{0}$ and covariance $(k-1)^{-1}\boldsymbol{I}$, with the combination of the linear approximation

$$H\left(\overline{\boldsymbol{x}}^b + \boldsymbol{X}^b \boldsymbol{w}\right) \approx \overline{\boldsymbol{y}}^b + \boldsymbol{Y}^b \boldsymbol{w} \tag{10}$$

where $\overline{\boldsymbol{y}}^b$ denote the mean of $\boldsymbol{y}^b$ ($\boldsymbol{y}^{b(i)} = H(\boldsymbol{x}^{b(i)})$), and matrix $\boldsymbol{Y}^b$ whose ith column is composed of $\boldsymbol{y}^{b(i)} - \overline{\boldsymbol{y}}^b$.

We can get the analysis.

$$\overline{\boldsymbol{w}}^a = \widetilde{\boldsymbol{P}}^a \left(\boldsymbol{Y}^b\right)^T \boldsymbol{R}^{-1} \left(\boldsymbol{y}^o - \overline{\boldsymbol{y}}^b\right),$$

$$\widetilde{\boldsymbol{P}}^a = \left[(k-1)\boldsymbol{I} + \left(\boldsymbol{Y}^b\right)^T \boldsymbol{R}^{-1} \boldsymbol{Y}^b\right]^{-1} \tag{11}$$

Finally, the analysis mean and covariance in the model space are

$$\overline{\boldsymbol{x}}^a = \overline{\boldsymbol{x}}^b + \boldsymbol{X}^b \overline{\boldsymbol{w}}^a$$

$$\boldsymbol{P}^a = \boldsymbol{X}^b \widetilde{\boldsymbol{P}}^a \left(\boldsymbol{X}^b\right)^T \tag{12}$$

In the actual implementation, we divided the global land into 51 regions according to the land cover and climate zones (Fig. S3). On the assumption that V_{cmax}^{25} of the same PFT in one region holds the same value, we made the optimization for each individual region, which could provide some insights into the spatial differences in V_{cmax}^{25}. This infrastructure is clearly distinguishable from that of Norton et al. (2019), in which they optimized the PFT-dependent V_{cmax}^{25} and other parameters

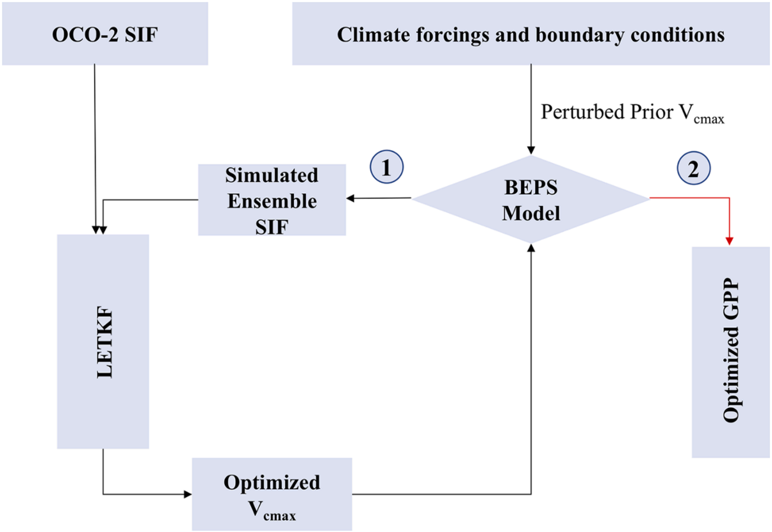

Fig. 1. Flowchart implemented in the assimilation system. There are two processes in one optimization step: (1) represents the first step to optimize the photosynthetic parameter (V_{cmax}^{25}), and (2) represents the second step to constrain the gross primary productivity (GPP) in the forward simulation based on the optimized V_{cmax}^{25}.

globally, without consideration of their variations.

Fig. 1 shows the flowchart implemented in GCAS. In one assimilation window (1 month) and one region, we first perturbed the default V_{cmax}^{25} in a Gaussian distribution based on the mean and standard deviation listed in the Table 1 to generate 20 ensembles. The mean and standard deviation values of V_{cmax}^{25} were mainly based on Chen et al. (2012). The BEPS model was then used to simulate the SIF distributions in 1 month based on the climate forcing, boundary conditions, and the generated 20 V_{cmax}^{25} ensembles. With the OCO-2 observed SIF in this month as the observation, the LETKF module was used to optimize V_{cmax}^{25}. We iterated this process in other regions. Finally, we used the optimized V_{cmax}^{25} to simulate the global GPP (posterior GPP) in a forward simulation.

2.4. Reference datasets used

We collected some other global GPP datasets to compare with the prior and posterior GPP distributions. Given that there are no 'true' datasets of global GPP, the datasets used here were employed for comparison rather than for evaluation. Six GPP datasets were used in this study. (1) The FLUXCOM RS GPP product which was generated using the site-based flux measurements and remoting sensing datasets via machine learning algorithms without the meteorological information (Tramontana et al., 2016). This dataset has the 0.5° × 0.5° horizontal resolution and 8-day time intervals. (2) The FluxSat GPP product that was based on satellite data within a simplified light-use efficiency (LUE) framework (Joiner et al., 2018). (3) Water, Energy and Carbon with Artificial Neural Networks (WECANN) Ver. 1.0, which is a global dataset containing the latent heat, sensible heat, and GPP based on the remote sensing observations, at 1° × 1° horizontal resolution on the monthly time scale (Alemohammad et al., 2017). (4) Monthly GPP from the MODIS MOD17 at 0.05° × 0.05° resolution (Zhao and Running, 2010). (5) GPP from the Vegetation Photosynthesis Model (VPM), which is based on the theory of an improved LUE and forced by related MODIS and NCEP Reanalysis 2 data (Zhang et al., 2017). (6) Multi-model simulated GPP in TRENDY v6 S3, in which all of models are driven by the same protocol, climate forcing, and land use datasets (Sitch et al., 2015). Additionally, we also collected the V_{cmax}^{25} values for seven PFTs from Kattge et al. (2009) to compare with the optimized V_{cmax}^{25}.

2.5. Validation at sites

In order to further verify whether the GPP prediction has been improved using the optimized V_{cmax}^{25} in this study, we independently performed the BEPS point simulations at several FLUXNET sites based on the default V_{cmax}^{25} and optimized V_{cmax}^{25}. Taking the PFTs at sites, focused PFTs in this text, and available observed GPP and climate forcing into account, we used observations from three sites (Table 2) to make the validation. We performed the simulations at these three sites from 2008 to 2012, neglecting the interannual variability of V_{cmax}^{25} because datasets in FLUXNET2015 (Pastorello et al., 2020) have no observations from 2015 to 2016. The BEPS point simulations here are driven by the climate observations at sites and MODIS LAI (Myneni et al., 2015).

3. Results

3.1. Optimization performance

To indicate whether the assimilation system works, we first present the comparisons among the OCO-2, prior, and posterior SIF in Fig. 2. The observed SIF has high values mainly in the regions of forests and croplands, such as over the Amazon, Central Africa, maritime continents, Eastern US, Eastern China, and Europe, with the maximum at approximately 1 W m^{-2} sr^{-1} μm^{-1} (Fig. 2a). The simulated prior SIF had the similar spatial patterns compared to the OCO-2 SIF (Fig. 2b). However, the strengths in prior SIF were clearly overestimated over the tropical

Table 2
FLUXNET sites used for quantitative validation for the GPP prediction improvements with the optimized V_{cmax}^{25}.

Site ID	Site Name	Latitude	Longitude	PFTs	Simulation Periods
FI-Hyy	Hyytiala	61.8474	24.2948	ENF	2008–2012
US-Ne2	Mead-irrigated maize-soybean rotation site	41.1649	−96.4701	Crop	2008–2012
US-Ne3	Mead-rainfed maize-soybean rotation site	41.1797	−96.4397	Crop	2008–2012

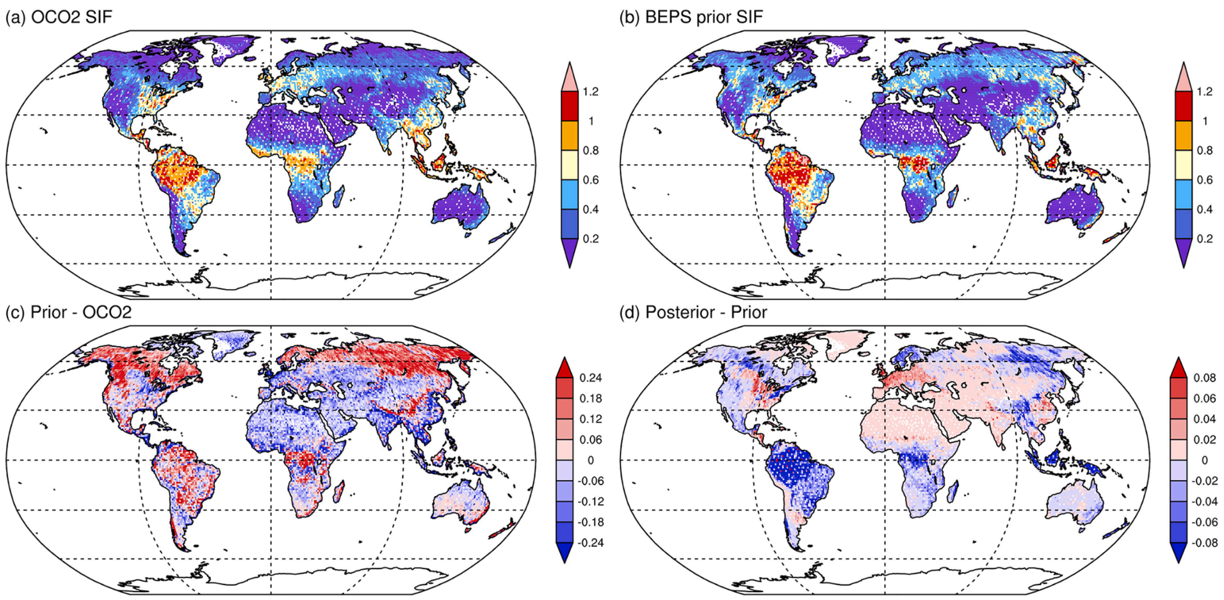

Fig. 2. Global distribution of the solar-induced chlorophyll fluorescence (SIF) in 2015–2016. (a) OCO-2 observation, (b) BEPS-simulated prior SIF, (c) difference between prior and OCO-2 SIF, and (d) difference between the posterior and prior SIF. The unit of SIF is W m^{-2} sr^{-1} μm^{-1}.

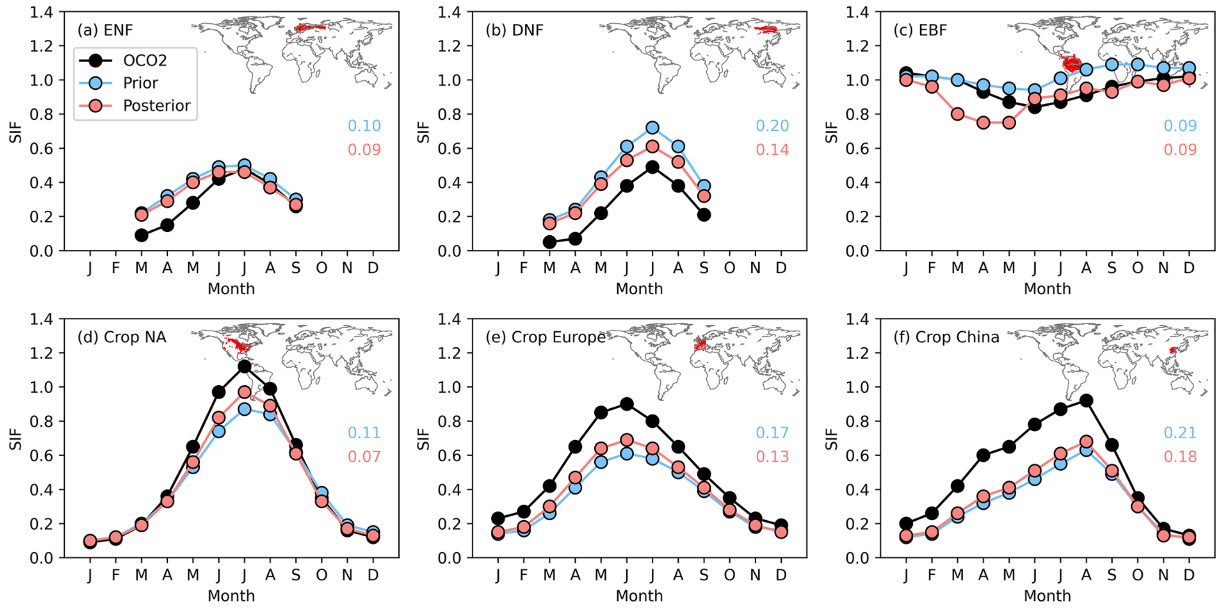

Fig. 3. SIF seasonal variations of different PFTs. (a) ENF, (b) DNF, (c) EBF, (d) Crop over North America, (e) Crop over Europe, and (f) Crop over North China. The black dots denote the OCO-2 SIF; the red dots denote the posterior SIF; the blue dots denote the prior values. All of them are smoothed by 3-month running average. The inset geographical maps in each figure show the averaged regions. The values in each figure denote the root mean square errors between OCO-2 SIF and prior (light blue)/posterior (light red). The SIF is in the unit of W m^{-2} sr^{-1} μm^{-1}. (For interpretation of the references to colour in this figure legend, the reader is referred to the web version of this article.)

and boreal forests, and Arctic tundra and shrubs (~0.2 W m^{-2} sr^{-1} μm^{-1}), and underestimated over the central of US, Eastern China, South Asia, and semi-arid and arid regions (Fig. 2c). After the optimization of V_{cmax}^{25}, the agreement of simulated SIF with OCO-2 observations was improved. The posterior SIF decreased/increased over the regions where overestimated/underestimated the values in prior (Fig. 2d). Compared with the prior SIF, the relative improvement of posterior SIF was about 5%–30% (Fig. S4).

Fig. 3 shows the comparisons of the SIF seasonal variations for different PFTs over specific forest and crop regions. The amplitudes of prior simulated SIF over the forest regions is somewhat higher than those of OCO-2 SIF (Figs. 2a, b, and c), whereas they are lower than OCO-2 SIF over crop regions (Figs. 2d, e, and f). These biases are consistent with the performance in the annual mean geographical distribution (Fig. 2c). In boreal spring, the prior simulated SIF values for ENF and DNF are clearly overestimated, showing an early growth cycle, which can be largely determined by the overestimated LAI. After the assimilation, the posterior SIF has been to some extent improved with the reduced root mean square errors (RMSE) between posterior and OCO2 SIF. However, it is also clear that biases induced by LAI datasets remains, suggesting that just optimizing V_{cmax}^{25} cannot rectify all the biases.

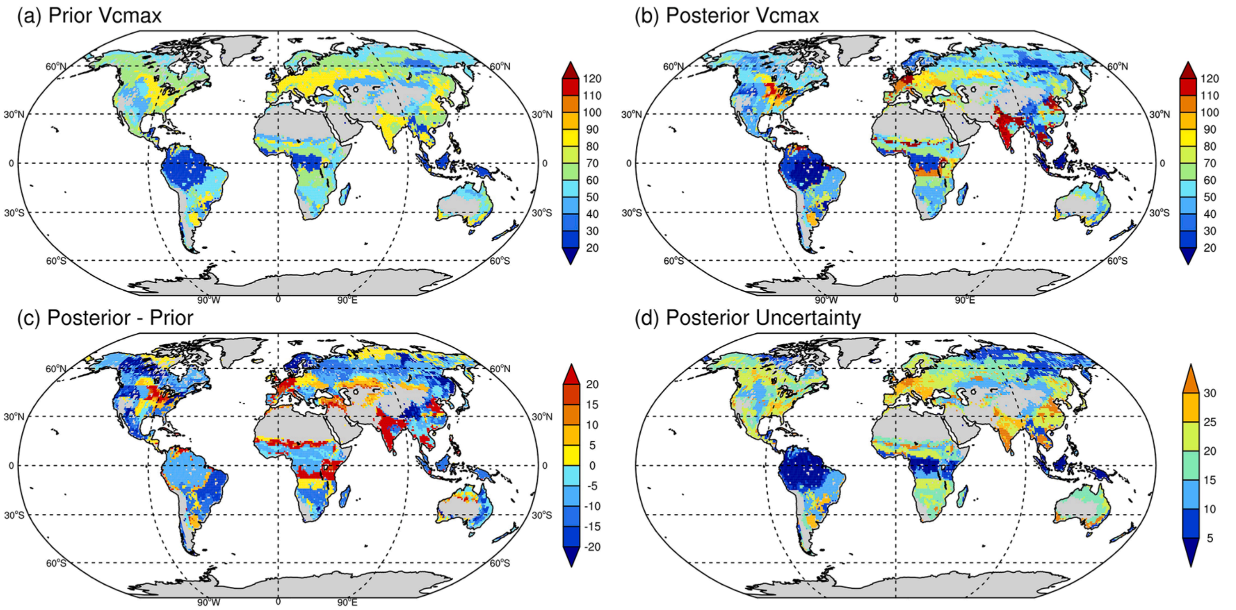

Fig. 4. Spatial distributions of the photosynthetic parameter (V_{cmax}^{25}). (a) Prior V_{cmax}^{25}, (b) Optimized V_{cmax}^{25}, (c) Difference between posterior and prior V_{cmax}^{25}, and (d) Uncertainties of the posterior V_{cmax}^{25}. V_{cmax}^{25} at each grid represents the value of dominant PFT. The V_{cmax}^{25} is in the unit of μmol $m^{-2}\ s^{-1}$.

All in all, this newly developed assimilation module can properly work, making the posterior SIF closer to the observations. It is a necessary prerequisite to further research on the optimized V_{cmax}^{25} and constrained GPP in the next context.

3.2. Optimized V_{cmax}^{25}

The PFT-dependent V_{cmax}^{25} is the state vector in the current assimilation module. Fig. 4 first presents the geographical distributions of optimized V_{cmax}^{25} against the prior values. As listed in Table 1, the prior V_{cmax}^{25} values are spatially diverse (Fig. 4a). The higher V_{cmax}^{25} values occur over the major crop regions (84.5 μmol $m^{-2}\ s^{-1}$, Table 1), such as North America, Europe, India, North China, and southeastern part of South America; the lowest V_{cmax}^{25} values occur over the tropical forests.

The spatial pattern of the optimized V_{cmax}^{25} is consistent with the prior spatial pattern, with the higher values over the major crop regions and lower values over the tropical and boreal forests (Fig. 4b). Specifically, the ENF V_{cmax}^{25} values are approximately 47.7 ± 22.4 μmol $m^{-2}\ s^{-1}$, and the DNF V_{cmax}^{25} are approximately 27.9 ± 8.8 μmol $m^{-2}\ s^{-1}$ (Fig. 4b and Fig. S1). These values are close to the estimates by He et al. (2019), who optimized V_{cmax}^{25} using sunlit GPP converted from remotely sensed SIF. Over the mix forests, the area-weighted average of optimized V_{cmax}^{25} is 59.4 ± 19.9 μmol $m^{-2}\ s^{-1}$. And the tropical EBF have the lowest V_{cmax}^{25} values (< 30 μmol $m^{-2}\ s^{-1}$). The V_{cmax}^{25} over the grass and shrub regions have the comparable amplitudes, with the values of 50.0 ± 13.6 and 52.7 ± 13.3 μmol $m^{-2}\ s^{-1}$, respectively (Fig. 4b and Fig. S1). These values over the grass and shrub regions are lower than the estimates in He et al. (2019). As for the crops, they have the highest but most variable V_{cmax}^{25} in space, owing to their different cropping systems. For example, the corn-soybean and wheat belts in US have the values of approximately 90–120 μmol $m^{-2}\ s^{-1}$; wheat-corn/wheat-soybean/wheat-peanut regions in North China and wheat-rice regions in Punjab, India have the values larger than 110 μmol $m^{-2}\ s^{-1}$. V_{cmax}^{25} over global crop regions is on average 97.6 ± 26.4 μmol $m^{-2}\ s^{-1}$, which is somewhat higher than the estimate of He et al. (2019) with the value of 82.7 ± 20.9 μmol $m^{-2}\ s^{-1}$.

Compared to the prior V_{cmax}^{25} values, we can see that optimized V_{cmax}^{25} values show somewhat reductions for the boreal and tropical forests (< −5 μmol $m^{-2}\ s^{-1}$; Fig. 4c). These regions are consistent with the higher SIF values relative to the OCO-2 SIF (Fig. 2c). In contrast, the obvious increase in optimized V_{cmax}^{25} occur over the major crop and grass lands (Fig. 4c), corresponding to the underestimated SIF over these regions (Fig. 2c). The optimized V_{cmax}^{25} in high Arctic tundra also shows a little increase, which is also revealed by He et al. (2019).

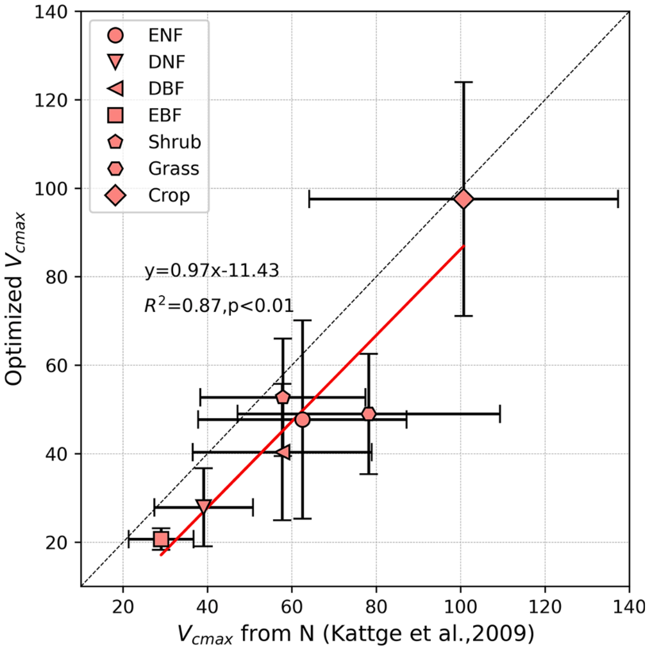

Fig. 5. Comparisons between optimized V_{cmax}^{25} and N-derived V_{cmax}^{25} (Kattge et al., 2009) for different PFTs. The error bars represent their respective uncertainties.

The uncertainties for optimized V_{cmax}^{25} are also shown in Fig. 4d. The lowest uncertainties occur over the tropical forests (< 5 μmol $m^{-2}\ s^{-1}$). The uncertainties over the DNF and high Arctic tundra regions also have the relatively lower values (<10 μmol $m^{-2}\ s^{-1}$). The highest uncertainties exist over the Europe, India, North China, and South America crop lands (> 25 μmol $m^{-2}\ s^{-1}$).

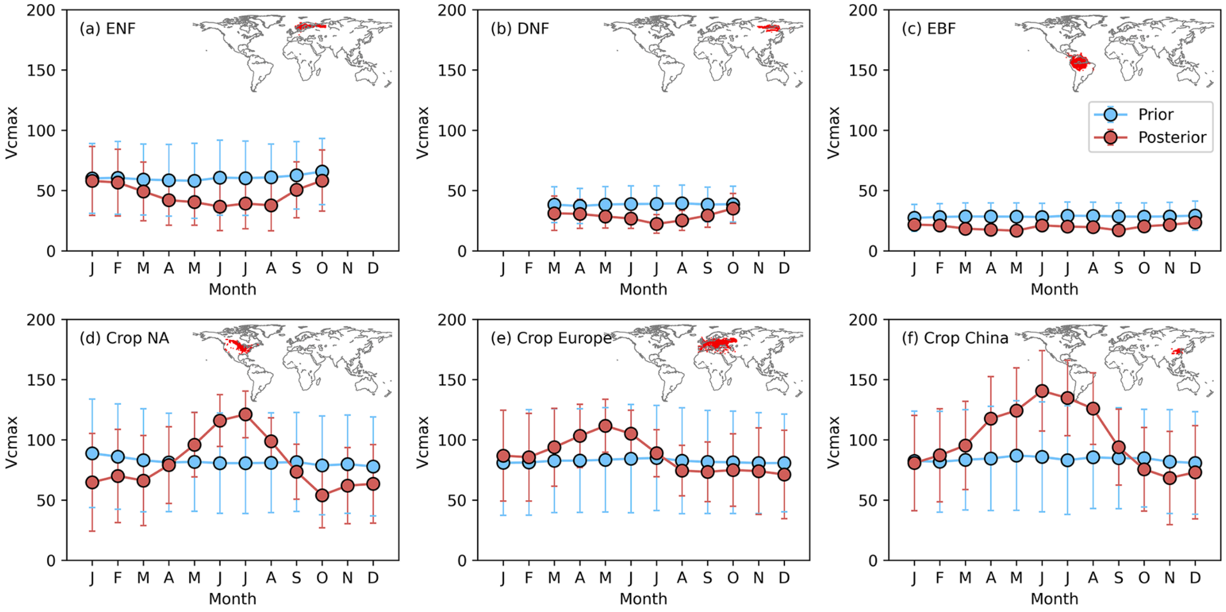

Fig. 6. V_{cmax}^{25} seasonal variations for different PFTs. (a) ENF, (b) DNF, (c) EBF, (d) Crop over North America, (e) Crop over Europe, and (f) Crop over North China. The Red dots denote the optimized V_{cmax}^{25} with their uncertainties; the blue dots denote the prior V_{cmax}^{25} with their uncertainties. Both of them are smoothed by 3-month running average. The inset geographical maps in each figure show the averaged regions. (For interpretation of the references to colour in this figure legend, the reader is referred to the web version of this article.)

Fig. 5 presents the comparison between optimized V_{cmax}^{25} and N-derived V_{cmax}^{25} for seven PFTs. They show the comparable amplitudes with the R^2 of 0.87 (Fig. 5). Because most of the default V_{cmax}^{25} except Mix, Grass, and Crop in BEPS (Table 1) refer to the values of Kattge et al. (2009), it simultaneously reflects the comparison between optimized and prior V_{cmax}^{25} to larger extent. Specifically, all of the optimized V_{cmax}^{25} except Crop are slightly weaker than N-derived values. The optimized V_{cmax}^{25} for Crop is 97.6 ± 26.4 μmol $m^{-2}s^{-1}$, obviously enhanced from

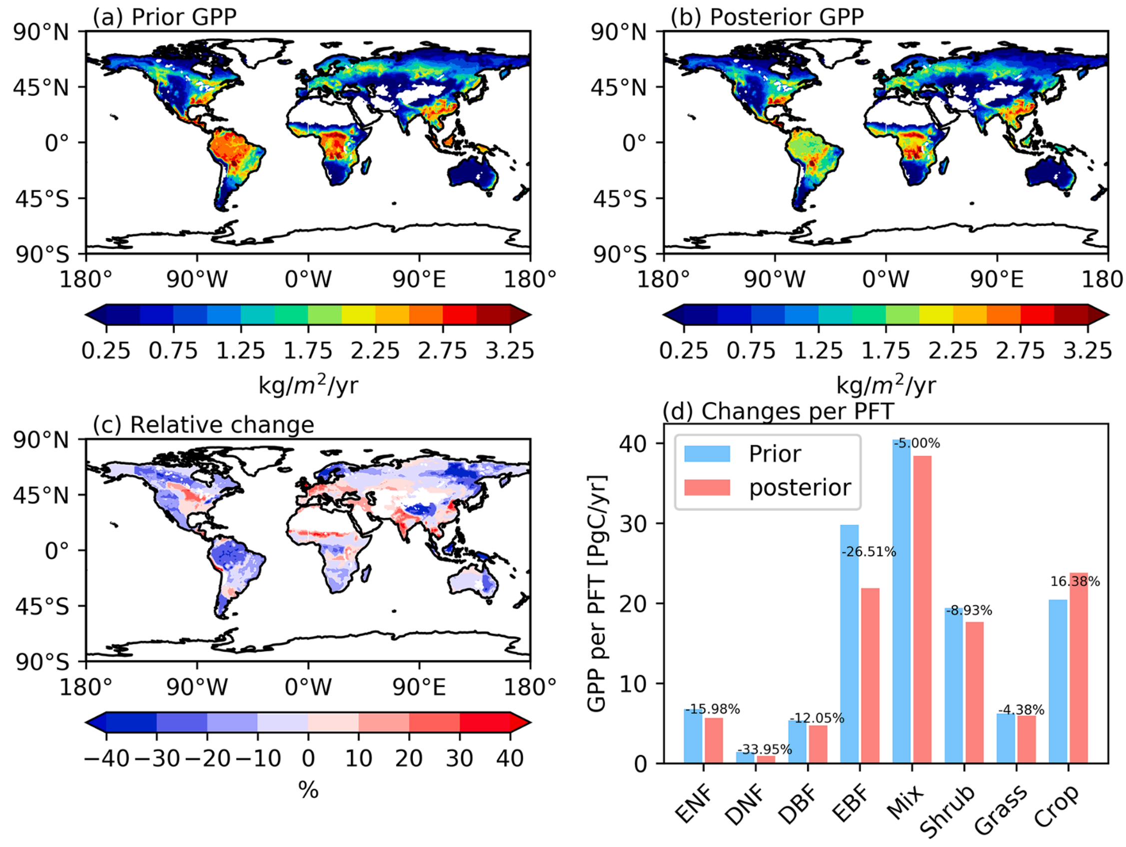

Fig. 7. Global distributions of gross primary productivity (GPP) in 2015–2016. (a) Prior GPP simulated by BEPS, (b) Constrained GPP, (c) Relative changes [%], and (d) Changes per PFT. The spatial GPP is in the unit of kg m^{-2} yr^{-1}.

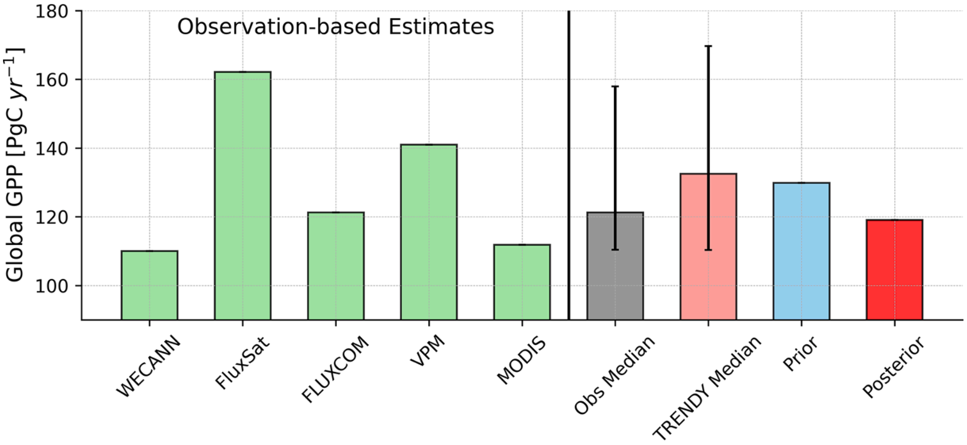

Fig. 8. Comparisons among observation-based estimated, TRENDYv6 simulated, prior, and posterior global total GPP in 2015–2016. The error bars for observation and TRENDY medians represent the 5% and 95% percentiles. The unit is PgC yr^{-1}.

the prior value (Table 1 and Fig. 4c), which is close to the N-derived C3 Crop value of 100.7 ± 36.6 μmol $m^{-2} s^{-1}$. Furthermore, the optimized V_{cmax}^{25} for all the PFTs show the reduced uncertainties compared to the N-derived values.

V_{cmax}^{25} can be greatly influenced by leaf nitrogen content and environmental factors such as temperature, humidity, and radiation (Ali et al., 2015; Hikosaka et al., 2006; Medlyn et al., 2002). Thus V_{cmax}^{25} can show significant seasonal and interannual variations. Fig. 6 illustrates the prior and posterior V_{cmax}^{25} seasonal variations for several specific PFTs over different regions. First of all, the prior V_{cmax}^{25} nearly keep the constant values all year round, because we perturbed the default V_{cmax}^{25} to generate the prior ensembles. Posterior V_{cmax}^{25} over the Amazon EBF shows unclear seasonal variations like the prior values (Fig. 6c). As for evergreen and deciduous needleleaf forests, the optimized V_{cmax}^{25} values show the higher values in boreal winter and spring and lower values in boreal summer (Figs. 6a and b). This behavior seems to be inconsistent with theoretical expectations that V_{cmax}^{25} would increase with temperature (Lin et al., 2013; Rogers et al., 2017b). Actually, it can be on the one hand largely influenced by our strategy in the assimilation process that we take the prior values as the posterior if there are not enough satellite-observed SIF (especially in winter) for the assimilation in each of 51 subregions (Fig. S3). On the other hand, it is associated with the underestimation of LAI in boreal winter and spring (He et al., 2019; Wang et al., 2016). Due to different cropping systems, the seasonal variations of V_{cmax}^{25} over different crop regions show some differences (Figs. 6d–f). The US agriculture belt, the single-cropping system, is characterized with the higher values in boreal summer (JJA) (Fig. 6d). The crops over Europe have the higher values in spring and early summer (winter wheat) (Fig. 6e). And the amplitudes are also close to the ground-based estimates for the maximum V_{cmax}^{25} for wheat with the values ranging from 105 to 150 μmol $m^{-2} s^{-1}$ (Silva-Perez et al., 2017; Sun et al., 2015). The North China, carrying out the double-cropping system, grows two dryland crops, such as the wheat-maize, wheat-peanut, or wheat-soybean. Basically, the wheat is sown in October, and harvested in the following year in June; the other crops are sown in June and harvested in October (Zhang et al., 2015b). Correspondingly, the optimized V_{cmax}^{25} here shows the long-lasting higher values during spring and summer (Fig. 6f).

3.3. Constrained GPP

We can constrain GPP in BEPS forward simulation using the optimized PFT-dependent V_{cmax}^{25}. The global distributions of the prior and posterior simulated GPP are shown in Figs. 7a and b. Though similar spatial patterns are evident, the regional amplitudes differ. Compared with the prior GPP, obvious increases in posterior GPP occur over the US agriculture belt, Europe, North China, India crop regions, and some of grasslands (Fig. 7c). Other regions show the decrease in posterior GPP. This relative change pattern of GPP is consistent with the changes in V_{cmax}^{25} (Fig. 4c). We can further compare the GPP values between prior and posterior for each PFT (Fig. 7d). All but crop show the reductions in posterior GPP. The reductions range from −34.0% for deciduous needleleaf forests to −4.4% for grass. In contrast, the posterior crop GPP increases by 16.4%.

Previous studies have estimated GPP on the basis of satellite observations, in situ measurements, and model simulations (Beer et al., 2010; Piao et al., 2013; Sitch et al., 2015; Zhao and Running, 2010). The comparisons among the prior, posterior, TRENDY v6 multi-model simulated, and observation-based estimated GPP in 2015–2016 are presented in Fig. 8. The estimates of the global GPP remain largely uncertain. In 5 observation-based estimates, the global total GPP ranges from 110.1 (WECANN) to 162.2 (FluxSat) PgC yr^{-1}, with their median of 121.3 PgC yr^{-1}. In TRENDY v6 15 state-of-the-art DGVM simulations, the global total GPP ranges from 104.0 (CLASS-CTEM) to 190.6 (ORCHIDEE) PgC yr^{-1}, with their median of 132.5 PgC yr^{-1} (Fig. 8). The prior simulated GPP in BEPS model is 129.9 PgC yr^{-1}, close to the median value of TRENDY v6 simulations. In contrast, after the assimilation, the posterior GPP decreases by 8.3% to 119.1 PgC yr^{-1}, which is close to the median value of the observation-based estimates.

The spatiotemporal variations in the optimized PFT-dependent V_{cmax}^{25} can reshape the seasonal cycle in GPP. Over the northern high latitudes (around 60°N), the posterior GPP during April to September decreases (Fig. 9c), corresponding to the decreases over the evergreen and deciduous needleleaf forests (Figs. 7c and d). During May to October, posterior GPP over the northern mid-latitudes increases (Fig. 9c), due to the GPP increases over the crop and grass lands (Figs.7c and d). Over the 20°S–5°N, posterior GPP basically decreases all year round.

3.4. Validation for GPP prediction improvements at sites

The optimized V_{cmax}^{25} shows significant seasonal variations, especially over crops (Fig. 6). We here independently performed BEPS point simulations at three sites (Crop: US-Ne2, US-Ne3, and ENF: FI-Hyy) to explore whether the optimized V_{cmax}^{25} can improve the GPP predictions to some extent. The rotation at US-Ne2 is characterized by the Mead-irrigated maize (C4)-soybean (C3) (Table 2). The BEPS model at this site with the default V_{cmax}^{25} underestimated the GPP predictions compared with the observations, showing the slope of 0.43 and RMSE of 2.85 (Fig. 10b). This GPP underestimation can result from the LAI bias over crop (Liu et al., 2018), constant V_{cmax}^{25}, and limitations of model

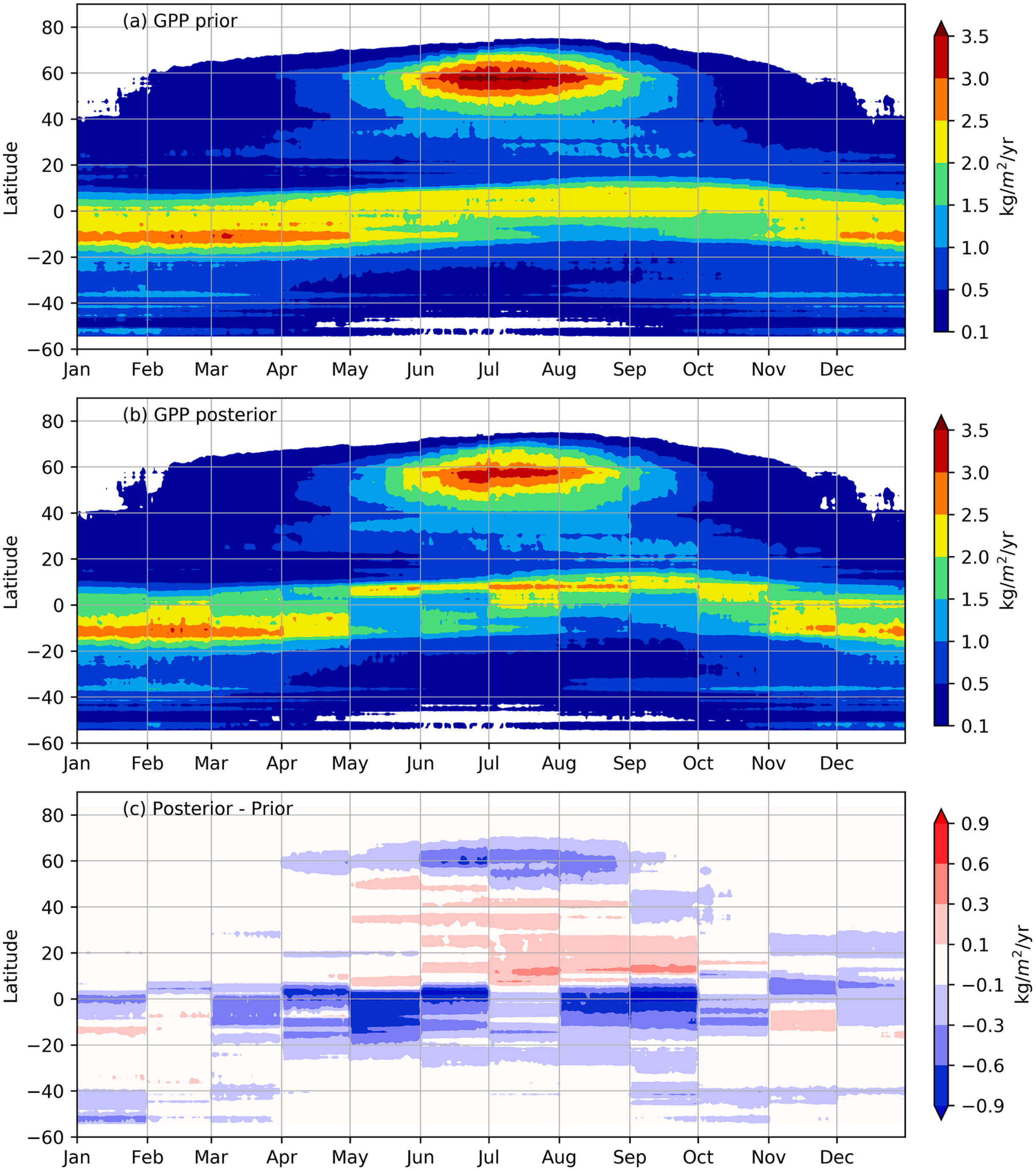

Fig. 9. Hovmöller diagrams of prior and posterior GPP. (a) Prior GPP, (b) Posterior GPP, and (c) Difference between posterior and prior.

processes (for example, irrigation and rotation from C4 to C3 photosynthesis pathway are not considered). Using the optimized V_{cmax}^{25}, model has better performance in GPP simulations with the slope of 0.49 and RMSE of 2.71 (Fig. 10b). At US-Ne3 site characterized by rainfed maize-soybean rotation (Table 2), BEPS can better simulate GPP with the default V_{cmax}^{25}, showing the slope of 0.58 and RMSE of 1.75. The GPP simulations can be further improved using the optimized V_{cmax}^{25}, with the RMSE of 1.65. At ENF site of FI-Hyy, GPP simulated with the optimized V_{cmax}^{25} are also better than those simulated with the default V_{cmax}^{25}, showing the reduced RMSE by 0.12. Therefore, the GPP simulations at these three sites are all improved using the optimized V_{cmax}^{25}, implying that the posterior V_{cmax}^{25} optimized by OCO-2 SIF can indeed constrain the terrestrial GPP simulations.

4. Discussion

4.1. Uncertainty in satellite observed SIF

Setting appropriate observational errors is critical in the assimilation system because it partially determines the distribution of the posterior result. Therefore, choices of the method to calculate SIF errors are important in the GPP optimization with SIF data as observation. There are several different methods used for estimating uncertainties of SIF: (1) The average of the single measurement precision error is calculated, which basically overestimates the uncertainty. (2) The standard error used in Parazoo et al. (2014) is to divide the average of the single measurement precision error by the square root of the number of

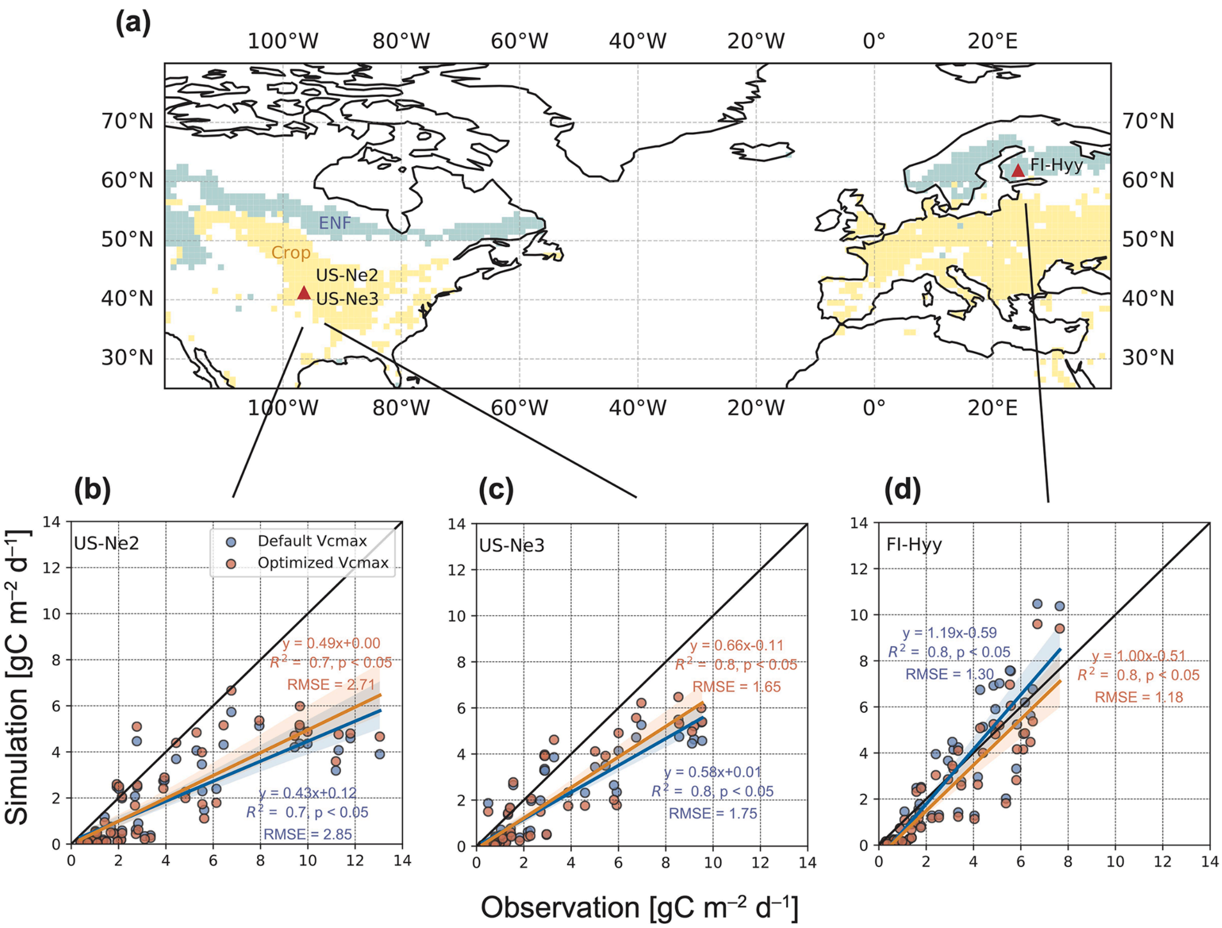

Fig. 10. Validations for the GPP prediction improvements with the optimized V_{cmax}^{25} at FLUXNET sites. (a) Spatial patterns for the dominant ENF (light blue) and Crop (yellow) PFTs associated with FLUXNET site locations. Comparisons between observed monthly GPP at sites and BEPS point simulations at US-Ne2 (b), US-Ne3 (c), and FI-Hyy (d) from 2008 to 2012. Simulations with the default and optimized V_{cmax}^{25} are in blue and tomato, respectively. The GPP is in the unit of gC m^{-2} d^{-1}.

observations. (3) The actual measured standard error of the mean is calculated as the standard deviation of the soundings in each grid divided by the square root of the number of observations (Sun et al., 2018). (4) Calculate the average of the single measurement precision errors and divide it by one half (Norton et al., 2019). Owing to their negligence of the systematic errors, the standard error and the actual measured standard error of the mean certainly underestimate the uncertainty. Therefore, we in this study basically adopt the method of Norton et al. (2019). However, it remains necessary to further investigate how to set the measurement errors of satellite-based SIF observations for their better use in the assimilation community.

4.2. Problems in parameter optimization

In terrestrial carbon cycle models, many factors influence the simulations, such as parameterization, process knowledge, acclimation, scaling (Rogers, 2014; Rogers et al., 2014, 2017a), model structures, uncertainties in meteorological drivers (Ito et al., 2017), and boundary forcing. For example, as in BEPS model, the uncertainty in satellite-derived LAI can exert large impact on GPP simulations (Liu et al., 2018). However, we here regard LAI as observations without uncertainties. Thus, limitations of model structures, uncertainties in other parameters (like LAI and clumping index) and forcing datasets would definitely influence the optimized parameters. A joint assimilation of SIF and other remotely sensed signals might be a solution for further constraining the variations of optimized parameters. Additionally, as mentioned above, our strategy in the assimilation process in which we take the prior values as the posterior if there are not enough satellite-observed SIF in each subregion for the assimilation can also induce uncertainties in the seasonal variations of optimized V_{cmax}^{25}. In the next work, one alternative choice may take the linearly extrapolated V_{cmax}^{25} from the optimized values in previous two months. Nevertheless, we proved the applicability of OCO-2 SIF data in improving the global GPP estimate through optimizing V_{cmax}^{25}.

4.3. Contrasting spatial patterns in V_{cmax}^{25}

Recently, several studies have demonstrated the spatial distributions of V_{cmax}^{25}, however, with contrasting patterns (Alton, 2018; He et al., 2019; Walker et al., 2017). Walker et al. (2017) predicted global V_{cmax}^{25} distributions based on four trait-scaling hypotheses (plant functional type, nutrient limitation, environmental filtering, and plant plasticity) with nine specific implementations. The markedly different means, variances, and latitudinal distributions exist in these nine global patterns of V_{cmax}^{25}. Almost all nutrient limitation hypothesis predicted moderate values in tropics, high values in the temperate zone, the highest values in dry temperate regions, and lowest values in the boreal zone before increasing in the high Arctic, while non-nutrient-based hypotheses tended to predict the opposite pattern with higher V_{cmax}^{25} in northern cool wet areas dominated by needleleaf PFTs and dry areas dominated by C3 grasses. Alton (2018) estimated the global V_{cmax}^{25} by combining MODIS LAI products with a hyperspectral index of total canopy chlorophyll concentration from the Medium Resolution Imaging Spectrometer (MERIS). The derived V_{cmax}^{25} have the highest values (55–60 μmol $m^{-2} s^{-1}$) in the mid-northern and mid-southern zones,

Table 3

Previous studies on the GPP optimization based on the satellite observed SIF datasets. The GPP here represents the global total values in the unit of PgC yr^{-1}.

No.	References	Methods	SIF dataset	GPP periods	Prior GPP	Posterior GPP	changes
1	Macbean et al., 2018	Linear relationship	GOME-2	2007–2011	194	166	−14.4%
2	He et al., 2019	Linear relationship	GOME-2	2007–2017	130.4	126.3	−3.1%
3	Norton et al., 2019	Process-based	OCO-2	2015	127.6	167	31%
4	Bacour et al., 2019	Process-based	OCO-2	1990–2009	162	134	−17.3%
5	This study	Process-based	OCO-2	2015–2016	129.9	119.1	−8.3%

corresponding to the C3 crops and grass. He et al. (2019) mapped the spatial variation of V_{cmax}^{25} by assimilating sunlit GPP converted from a 11-yearlong satellite-observed SIF. Interestingly, they revealed a very high V_{cmax}^{25} regions in South America associated with the rapid development of soybean cultivation in recent years. Comparing to these spatial distributions, the optimized V_{cmax}^{25} in this study resembles the spatial pattern of Alton (2018) with the highest values over the C3 crop regions. However, in general, optimized V_{cmax}^{25} shows the higher amplitudes (Fig. 4b).

4.4. Status quo in constraining gpp based on the satellite observed SIF

As we know, terrestrial GPP amplitudes estimated by different methods, such as satellite-based estimates, in situ measurements upscaling, and model simulations (Beer et al., 2010; Joiner et al., 2018; Jung et al., 2011; Piao et al., 2013; Sitch et al., 2015; Zhao and Running, 2010) have large uncertainties. Therefore, we constrained the terrestrial GPP estimate with OCO-2 SIF observations on the basis of the effectiveness of SIF in indicating GPP (Guanter et al., 2014). Table 3 summaries outputs from some recent studies optimizing GPP with SIF data. Macbean et al. (2018) and He et al. (2019) utilized the linear relationship to constrain GPP based on the GOME-2 SIF, making the posterior GPP have the values of 166 and 126.3 PgC yr^{-1}, respectively. Additionally, Parazoo et al. (2014) used the GOSAT SIF data to constrain global GPP based on the linear relationship, pointing out that a redistribution of GPP occurred with the reduction in northern forests (~3.6 PgC yr^{-1}) and enhancement in tropical forests (~3.7 PgC yr^{-1}). In contrast, Norton et al. (2019) and Bacour et al. (2019) utilized the process-based SIF model to constrain global GPP based on the OCO-2 SIF. Their posterior GPP have the values of 167 and 134 PgC yr^{-1}, respectively. In this study, we also constrained the global GPP using the OCO-2 SIF in a process-based manner, with the posterior GPP of 119.1 PgC yr^{-1}. Based on these results, we can find out that the global GPP amplitudes do not converge, though all of the studies utilized the information of the satellite observed SIF data. It seems that the results depend on the prior conditions, structures of the assimilation system, settings of the uncertainties of the SIF data, and etc. However, the posterior GPP in most of researches showed somewhat reductions compared to the prior simulated GPP (Table 3).

5. Concluding remarks

Recent satellite-based SIF datasets contain information on the spatiotemporal patterns of terrestrial GPP. In this study, we first utilized OCO-2 SIF in a global carbon assimilation system to optimize the PFT-dependent V_{cmax}^{25}, and then used the optimized V_{cmax}^{25} to constrain the terrestrial GPP on the regional and global scales. The main conclusions are as follows:

(1)The optimized V_{cmax}^{25} has the largest values over the major crop regions, such as the US agriculture belt, Europe, India, North China. Compared with the prior values, optimized V_{cmax}^{25} over the croplands and some of grasslands increase, while they decrease over the tropical and boreal forests. Importantly, the optimized V_{cmax}^{25} of different PFTs show clear seasonal variations. Over the different croplands, the seasonal variations show some differences, owing to their different cropping systems. The US agriculture belt, the single-cropping system, is characterized with the higher values in summer; the crops over Europe have the higher V_{cmax}^{25} in spring and then decline; the optimized V_{cmax}^{25} over the North China shows a long-lasting higher values in spring and summer.

(2)Compared with the prior simulation, the constrained global GPP in 2015–2016 was reduced by 10.8 PgC yr^{-1}, or 8.3% to 119.1 PgC yr^{-1}, more consistent with the median of 121.3 PgC yr^{-1} in the observation-based estimates. Regionally, GPP increases over the major croplands and some of grasslands, while it decreases over the other regions. GPP of crop increases by 16.4%. And the reductions range from −34.0% for deciduous needleleaf forests to −4.4% for grass. The seasonal variation of GPP is also reshaped by optimized V_{cmax}^{25} with its spatiotemporal variation. The constrained GPP from April to September decreases over the northern high latitudes, while it increases from May to October over the northern mid-latitudes. Over the 20°S–5°N, the constrained GPP basically decreases all year round.

Declaration of Competing Interest

The authors declare that they have no known competing financial interests or personal relationships that could have appeared to influence the work reported in this paper.

Acknowledgements

This study was supported by the National Key R&D Program of China (grant no. 2016YFA0600204), National Natural Science Foundation of China (grant no. 41807434, 41605039, 41871334), the Fundamental Research Funds for the Central Universities (0904-14380028). Jun Wang (201906195014) thank the China Scholarship Council for funding. We are grateful to the High Performance Computing Center (HPCC) of Nanjing University for doing the numerical calculations in this paper on its blade cluster system.

Supplementary materials

Supplementary material associated with this article can be found, in the online version, at doi:10.1016/j.agrformet.2021.108424.

References

Alemohammad, S.H., et al., 2017. Water, Energy, and Carbon with Artificial Neural Networks (WECANN): a statistically based estimate of global surface turbulent fluxes and gross primary productivity using solar-induced fluorescence. Biogeosciences 14 (18), 4101–4124.

Ali, A.A., et al., 2015. Global-scale environmental control of plant photosynthetic capacity. Ecol. Appl. 25 (8), 2349–2365.

Alton, P.B., 2018. Decadal trends in photosynthetic capacity and leaf area index inferred from satellite remote sensing for global vegetation types. Agric. For. Meteorol. 250-251, 361–375.

Bacour, C. et al., 2019. Improving estimates of Gross Primary Productivity by assimilating solar-induced fluorescence satellite retrievals in a terrestrial biosphere model using a process-based SIF model. Journal of Geophysical Research: Biogeosciences.

Beer, C., et al., 2010. Terrestrial Gross Carbon Dioxide Uptake: global Distribution and Covariation with Climate. Science 329 (5993), 834–838.

Chen, J.M., Liu, J., Cihlar, J., Goulden, M.L., 1999. Daily canopy photosynthesis model through temporal and spatial scaling for remote sensing applications. Ecol. Modell. 124, 99–119.

Chen, J.M., et al., 2012. Effects of foliage clumping on the estimation of global terrestrial gross primary productivity. Glob. Biogeochem. Cycles 26 (1), GB1019.

Damm, A., et al., 2015. Far-red sun-induced chlorophyll fluorescence shows ecosystem-specific relationships to gross primary production: an assessment based on observational and modeling approaches. Remote Sens. Environ. 166, 91–105.

Dee, D.P., et al., 2011. The ERA-Interim reanalysis: configuration and performance of the data assimilation system. Q. J. R. Meteorolog. Soc. 137 (656), 553–597.

Farquhar, G.D., von Caemmerer, S., Berry, J.A., 1980. A biochemical model of the photosyntheric assimilation in C3 species. Planta 149, 78–90.

Frankenberg, C., et al., 2011. New global observations of the terrestrial carbon cycle from GOSAT: patterns of plant fluorescence with gross primary productivity. Geophys. Res. Lett. 38.

Genty, B., Briantais, J.M., Baker, N.R., 1989. The Relationship between the Quantum Yield of Photosynthetic Electron-Transport and Quenching of Chlorophyll Fluorescence. Biochim. Biophys. Acta 990 (1), 87–92.

Guanter, L., et al., 2014. Global and Time-Resolved Monitoring of Crop Photosynthesis With Chlorophyll Fluorescence. PNAS, pp. E1327–E1333.

He, L., et al., 2019. Diverse photosynthetic capacity of global ecosystems mapped by satellite chlorophyll fluorescence measurements. Remote Sens. Environ. 232.

Hikosaka, K., Ishikawa, K., Borjigidai, A., Muller, O., Onoda, Y., 2006. Temperature acclimation of photosynthesis: mechanisms involved in the changes in temperature dependence of photosynthetic rate. J. Exp. Bot. 57 (2), 291–302.

Hilton, T.W., 2018. Photosynthesis in high definition. Nat Clim Chang 8 (1), 20–21.

Hunt, B.R., Kostelich, E.J., Szunyogh, I., 2007. Efficient data assimilation for spatiotemporal chaos: a local ensemble transform Kalman filter. Physica D 230 (1–2), 112–126.

Huntzinger, D.N., et al., 2012. North American Carbon Program (NACP) regional interim synthesis: terrestrial biospheric model intercomparison. Ecol. Modell. 232, 144–157.

Ito, A., et al., 2017. Photosynthetic productivity and its efficiencies in ISIMIP2a biome models: benchmarking for impact assessment studies. Environ. Res. Lett. 12 (8).

Joiner, J., et al., 2011. First observations of global and seasonal terrestrial chlorophyll fluorescence from space. Biogeosciences 8 (3), 637–651.

Joiner, J., et al., 2018. Estimation of Terrestrial Global Gross Primary Production (GPP) with Satellite Data-Driven Models and Eddy Covariance Flux Data. Remote Sens (Basel) 10 (9).

Jung, M., et al., 2011. Global patterns of land-atmosphere fluxes of carbon dioxide, latent heat, and sensible heat derived from eddy covariance, satellite, and meteorological observations. J Geophys Res-Biogeo 116.

Kattge, J., Knorr, W., Raddatz, T., Wirth, C., 2009. Quantifying photosynthetic capacity and its relationship to leaf nitrogen content for global-scale terrestrial biosphere models. Glob Chang Biol 15 (4), 976–991.

Koffi, E.N., Rayner, P.J., Norton, A.J., Frankenberg, C., Scholze, M., 2015. Investigating the usefulness of satellite-derived fluorescence data in inferring gross primary productivity within the carbon cycle data assimilation system. Biogeosciences 12 (13), 4067–4084.

Lin, Y.S., Medlyn, B.E., De Kauwe, M.G., Ellsworth, D.S., 2013. Biochemical photosynthetic responses to temperature: how do interspecific differences compare with seasonal shifts? Tree Physiol. 33 (8), 793–806.

Liu, Y., Liu, R.G., Chen, J.M., 2012. Retrospective retrieval of long-term consistent global leaf area index (1981-2011) from combined AVHRR and MODIS data. J Geophys Res-Biogeo 117.

Liu, Y., et al., 2018. Satellite-derived LAI products exhibit large discrepancies and can lead to substantial uncertainty in simulated carbon and water fluxes. Remote Sens. Environ. 206, 174–188.

MacBean, N., et al., 2018. Strong constraint on modelled global carbon uptake using solar-induced chlorophyll fluorescence data. Sci Rep-Uk 8 (1).

Medlyn, B.E., et al., 1999. Effects of elevated [CO2] on photosynthesis in European forest species: a meta-analysis of model parameters. Plant Cell and Environment 22 (12), 1475–1495.

Medlyn, B.E., et al., 2002. Temperature response of parameters of a biochemically based model of photosynthesis. II. A review of experimental data. Plant Cell Environ. 25, 1167–1179.

Myneni, R., Knyazikhin, Y., Park, T., 2015. MCD15A2H MODIS/Terra+Aqua Leaf Area Index/FPAR 8-day L4 Global 500m SIN Grid V006. NASA EOSDIS Land Processes. DAAC. https://doi.org/10.5067/MODIS/MCD15A2H.006.

Norman, J.M., 1982. Simulation of microclimates, in Biometeorology in Integrated Pest Management, in: J. L. Hatfield and I. J. Thomason (Eds.), pp. 65–99, Academic, San Diego, Calif.

Norton, A.J., et al., 2019. Estimating global gross primary productivity using chlorophyll fluorescence and a data assimilation system with the BETHY-SCOPE model. Biogeosciences 16 (15), 3069–3093.

Parazoo, N.C., et al., 2014. Terrestrial gross primary production inferred from satellite fluorescence and vegetation models. Glob Chang Biol 20 (10), 3103–3121.

Pastorello, G., et al., 2020. The FLUXNET2015 dataset and the ONEFlux processing pipeline for eddy covariance data. Sci Data 7 (1), 225.

Peters, W., et al., 2007. An atmospheric perspective on North American carbon dioxide exchange: carbonTracker. Proc. Natl. Acad. Sci. U. S. A. 104 (48), 18925–18930.

Piao, S. et al., 2013. Evaluation of terrestrial carbon cycle models for their response to climate variability and to CO2trends. Glob Chang Biol: 2117–2132.

Qiu, B., Chen, J.M., Ju, W., Zhang, Q., Zhang, Y., 2019. Simulating emission and scattering of solar-induced chlorophyll fluorescence at far-red band in global vegetation with different canopy structures. Remote Sens. Environ. 233.

Rogers, A., 2014. The use and misuse of V(c,max) in Earth System Models. Photosynth. Res. 119 (1–2), 15–29.

Rogers, A., Medlyn, B.E., Dukes, J.S., 2014. Improving representation of photosynthesis in Earth System Models. New Phytol. 204, 12–14.

Rogers, A., et al., 2017a. A roadmap for improving the representation of photosynthesis in Earth system models. New Phytol. 213 (1), 22–42.

Rogers, A., Serbin, S.P., Ely, K.S., Sloan, V.L., Wullschleger, S.D., 2017b. Terrestrial biosphere models underestimate photosynthetic capacity and CO2 assimilation in the Arctic. New Phytol. 216 (4), 1090–1103.

Silva-Perez, V., Furbank, R.T., Condon, A.G., Evans, J.R., 2017. Biochemical model of C3 photosynthesis applied to wheat at different temperatures. Plant Cell Environ. 40 (8), 1552–1564.

Sitch, S., et al., 2015. Recent trends and drivers of regional sources and sinks of carbon dioxide. Biogeosciences 12 (3), 653–679.

Sun, J., Sun, J., Feng, Z., 2015. Modelling photosynthesis in flag leaves of winter wheat (Triticum aestivum) considering the variation in photosynthesis parameters during development. Functional Plant Biology 42 (11).

Sun, Y., et al., 2018. Overview of Solar-Induced chlorophyll Fluorescence (SIF) from the Orbiting Carbon Observatory-2: retrieval, cross-mission comparison, and global monitoring for GPP. Remote Sens. Environ. 209, 808–823.

Tramontana, G., et al., 2016. Predicting carbon dioxide and energy fluxes across global FLUXNET sites with regression algorithms. Biogeosciences 13 (14), 4291–4313.

van der Tol, C., Berry, J.A., Campbell, P.K., Rascher, U., 2014. Models of fluorescence and photosynthesis for interpreting measurements of solar-induced chlorophyll fluorescence. J. Geophys. Res. Biogeosci. 119 (12), 2312–2327.

Walker, A.P., et al., 2017. The impact of alternative trait-scaling hypotheses for the maximum photosynthetic carboxylation rate (Vcmax) on global gross primary production. New Phytol. 215 (4), 1370–1386.

Wang, R., Chen, J.M., Pavlic, G., Arain, A., 2016. Improving winter leaf area index estimation in coniferous forests and its significance in estimating the land surface albedo. ISPRS J. Photogramm. Remote Sens. 119, 32–48.

Weis, E., Berry, J., 1987. Quantum efficiency of photosystem II in reation to energy-dependent quenching of chlorophyll fluorescence. Biochim. Biophys. Acta 894, 198–208.

Yang, X., et al., 2015. Solar-induced chlorophyll fluorescence that correlates with canopy photosynthesis on diurnal and seasonal scales in a temperate deciduous forest. Geophys. Res. Lett. 42 (8), 2977–2987.

Zhang, S. et al., 2014a. Global carbon assimilation system using a local ensemble Kalman filter with multiple ecosystem models. Journal of Geophysical Research: Biogeosciences, 119(11): 2171–2187.

Zhang, S., et al., 2015a. A global carbon assimilation system using a modified ensemble Kalman filter. Geosci Model Dev 8 (3), 805–816.

Zhang, W., Zheng, C., Song, Z., Deng, A., He, Z., 2015b. Farming systems in China: innovations for sustainable crop production. Crop Physiology 43–64.

Zhang, Y., et al., 2014b. Estimation of vegetation photosynthetic capacity from space-based measurements of chlorophyll fluorescence for terrestrial biosphere models. Glob Chang Biol 20, 3727–3742.

Zhang, Y., Guanter, L., Joiner, J., Song, L., Guan, K., 2018. Spatially-explicit monitoring of crop photosynthetic capacity through the use of space-based chlorophyll fluorescence data. Remote Sens. Environ. 210, 362–374.

Zhang, Y., et al., 2017. A global moderate resolution dataset of gross primary production of vegetation for 2000-2016. Sci Data 4, 170165.

Zhang, Z., et al., 2020. Reduction of structural impacts and distinction of photosynthetic pathways in a global estimation of GPP from space-borne solar-induced chlorophyll fluorescence. Remote Sens. Environ. 240.

Zhao, M., Running, S.W., 2010. Drought-induced reduction in global terrestrial net primary production from 2000 through 2009. Science 329 (5994), 940–943.